

# Multistage micro-structured ionic skin for real-time vital signs monitoring and human-machine interaction

Xueke Wang<sup>1</sup>, Jinyu Zi<sup>1</sup>, Yi Chen<sup>1</sup>, Qiang Wu<sup>1</sup>, Zhimin Xiang<sup>1</sup>, Yongqiang Tu<sup>1</sup>, Peng Yang<sup>1</sup>, and Yanfen Wan<sup>1</sup>

<sup>1</sup>Yunnan University

April 14, 2024

## Abstract

Skin-like electronics research aiming to mimic even surpass human-like specific tactile cognition by operating perception-to-cognition-to-feedback of stimulus to build intelligent cognition systems for certain imperceptible or inappreciable signals was so attractive. Herein, we constructed an all-in-one wearable device to address the sensitivity and power supply simultaneously by integrating multistage micro-structured ionic skin (MM i-skin) and piezoelectric & thermoelectric dual-mode self-power staffs. The MM i-skin with multi-stage “interlocked” configurations achieved precise recognition of subtle signals, where the sensitivity reached up to 77.4 kPa<sup>-1</sup>, as well as response time of 46 ms, cyclic stability (over 1500 cycles), and a pressure detection limit (over 50 kPa). Furthermore, we developed a piezo/thermo-electricity dual-mode nanogenerator, denoted as P-iskin / T-iskin, for self-powering the pressure sensor. This self-powered multifunctional ionic skin enables real-time monitoring of weak body signals, rehab guidance, and robotic motion recognition, demonstrating potential for internet of things (IoT) applications involving the artificial intelligence-motivated sapiential healthcare internet (SHI) and widely distributed human-machine interaction (HMI).

Article category: Research Article

Subcategory: Thermoelectricity, piezoelectricity, self-powered sensing

Multistage micro-structured ionic skin for real-time vital signs monitoring and human-machine interaction

Xueke Wang, Jinyu Zi, Yi Chen, Qiang Wu, Zhimin Xiang, Yongqiang Tu, Peng Yang, Yanfen Wan\*

X. Wang, J. Zi, Y. Chen, Q. Wu, Z. Xiang, Y. Tu, Dr. P. Yang, Prof. Y. Wan

National Center for International Research on Photoelectric and Energy Materials, Yunnan Key Laboratory for Micro/Nano Materials & Technology, Yunnan Key Laboratory of Electromagnetic Materials and Devices, School of Materials and Energy, Yunnan University, Kunming 650091, China.

E-mail: [yfwan@ynu.edu.cn](mailto:yfwan@ynu.edu.cn)

Keywords: skin-like microstructure, bio-template method, ionic skin, dual-mode self-power, integrated device

Abstract:

Skin-like electronics research aiming to mimic even surpass human-like specific tactile cognition by operating perception-to-cognition-to-feedback of stimulus to build intelligent cognition systems for certain imperceptible or inappreciable signals was so attractive. Herein, we constructed an all-in-one wearable device to address the sensitivity and power supply simultaneously by integrating multistage micro-structured ionic skin (MM i-skin) and piezoelectric & thermoelectric dual-mode self-power staffs. The MM i-skin with multi-stage “interlocked” configurations achieved precise recognition of subtle signals, where the sensitivity reached up to 77.4 kPa<sup>-1</sup>, as well as response time of 46 ms, cyclic stability (over 1500 cycles), and a pressure detection limit

(over 50 kPa). Furthermore, we developed a piezo/thermo-electricity dual-mode nanogenerator, denoted as P-iskin / T-iskin, for self-powering the pressure sensor. This self-powered multifunctional ionic skin enables real-time monitoring of weak body signals, rehab guidance, and robotic motion recognition, demonstrating potential for internet of things (IoT) applications involving the artificial intelligence-motivated sapiential healthcare internet (SHI) and widely distributed human-machine interaction (HMI).

## 1. Introduction

Humans are considered as the smartest creatures on earth, but actually animals and plants have more superpower far surpassing humans in some abilities, one of which is the sense of touch.<sup>[1,2]</sup> Some animals possess an incredible tactile sensation which covers more than the sensation of pressure, heat, texture, and even pain between an object and the skin.<sup>[3]</sup> Like the extra-sensitive skin of crocodile with many protruding black spots on their scales called the dome pressure receptor or the outer skin sensory organ, which is as sensitive as a finger.<sup>[4]</sup> In addition, plants also have a sense of touch, and they can even “perceive” when their leaves are picked or attacked, Like mimosa will droop petioles and close its small leaves as “shyness” when touched by the outside world.<sup>[5]</sup> Each life entity has similar sensory organs which can be interpreted as perceiving physical/chemical information about their surroundings, noted as tactile.<sup>[3]</sup> The previous biology studies have found that the skin of humans and higher animals consists of three layers: epidermis, dermis, and subcutaneous tissue, where the intromission with “interlocked” configurations are existed between epidermis-dermis and dermis-subcutaneous tissue.<sup>[6,7]</sup> Benefiting from these interleaved interlocked layer, the weak stimuli could be perceived and amplified to obtain esthesia through this tactile sensor quickly.<sup>[8-10]</sup> From the above-mentioned relationship between sensing properties and interlocked structure, real skin provides a great imaginary space for us to imitate and develop artificial perception organ such as electronic skin (e-skin),<sup>[11]</sup> ionic skin(i-skin),<sup>[12]</sup> artificial limb,<sup>[13]</sup> soft robots<sup>[14]</sup> or brain computer interface (BCI),<sup>[15]</sup> which are called for potentializing numerous internet of things (IoT) applications involving the artificial intelligence (AI) -motivated sapiential healthcare internet (SHI),<sup>[16]</sup> intelligent cognition systems (ICS),<sup>[17]</sup> and widely distributed human-machine interaction (HMI).<sup>[18]</sup>

Tactile-like wearable electronics advanced rapidly in recent years with unique characteristics of perception-to-cognition-to-feedback external stimulus to build intelligent cognition systems which could mimic humans and higher animals-like specific tactile cognition. Advances in wearable sensors, flexible circuit integration techniques now allow e-skin and i-skin to detect key physiological indicators such as pulse, heartbeat, body motion, and certain inappreciable signals. Among diverse sensors, the capacitive pressure sensors are very attractive for its superior performance of expeditious responding and amplifying the local press stimuli and thus enable to feedback outside stimulus information instantaneously. In recent years, aiming to improve the compressibility and sensitivity of sensors to detect very weak signals, most of capacitive pressure sensors are focused on introducing micro-nano structures like pyramids,<sup>[19]</sup> microspheres,<sup>[20]</sup> nanowires,<sup>[21]</sup> layered structures,<sup>[22]</sup> and interlocked structures.<sup>[23]</sup> But the further research on multi-stage interlocked microstructures related to the tactile perception performance is rare. So, for clearly illuminating the correlative dependence of sensing properties on microstructure, researchers try to explore another new microstructure derived from nature to artificial staff, not only for enhanced sensitivity but also for exploiting simple preparation technology. Besides artificial templates, plants like lotus were also selected as templates for multi-level microstructures of the flexible electrode layer or dielectric layer.<sup>[24-26]</sup>

However, it still remains a huge space to improve the degree of sensitivity, response capacity, and device stability to satisfy the monitoring of subtle physiological signals especially. And simultaneously it needs address another challenge how to drive and sustainably operate the device with wireless and low consume power supply?

Currently, using substantial extra rigid energy-driving with limited-service lifetime, and inadequate flexible circuit entangled it into dilemma of actual application. So, it calls for wearable energy harvesters for resolving the wearable power supply issue where various types of surrounding or tight-fitting energy sources could be

converted into electricity. The transformed electricity not only could directly act as active sensing signals of physiological parameters but also could power additional sensors as well as signal processing and data delivery. Emerging self-powered sensor systems integrating sensors with self energy-power management module could operate sustainably without an external power supply which absolutely are advantageous candidates in the next generation of intelligent wearable flexible electronics. What’s more, researchers have proposed the concept of in-situ utilization of low-order thermal and mechanical energy of body to convert it into electrical energy such as piezoelectricity,<sup>[27]</sup> triboelectric,<sup>[28]</sup> thermoelectricity,<sup>[29]</sup> hydrovoltaic power,<sup>[30]</sup> and humidity power.<sup>[31]</sup> The surroundings is full of low-order energy and heat variation,<sup>[32]</sup> which makes it possible to convert it into electricity using thermoelectric material to power pressure sensors, but there has been uncared for it.

Traditional thermoelectric materials are mainly inorganic semiconductor materials composed of covalent/ionic bonds, which have intrinsic rigidity and are not prone to flexible deformation.<sup>[33,34]</sup> In practical applications, it is difficult to fit closely with the heat source surface with complex curvature changes, which is easy to cause poor thermal contact, resulting in the reduction of conversion efficiency or temperature control accuracy/sensitivity. In contrast, ionogel, as a new type of thermoelectric material, became a new hot spot due to superior electrical conductivity and thermoelectricity, as well as excellent self-healing and shape memory properties, which makes ionogel an ideal ion skin sensing candidate.<sup>[35-37]</sup> However, compared with a large amount of work conducted on the strength, self-healing, and high tensile properties of ionogel by many researchers, research on the thermoelectric properties of ionogel is relatively limited, and the development of thermoelectric ionogel that collecting body heat to enable self-powered ionic skin sensing for real-time monitoring of human-related activities has been relatively rare so far. In addition to thermoelectric properties, the piezoelectric properties of ionogel have been vigorously investigated. Shen et al. prepared an electrical double layer (EDL) capacitive ion pressure sensor by exploiting the outstanding ionic conductivity of the ionogel, and the pressure sensor sensitivity was about 44 times higher than that of a traditional parallel-plate capacitor.<sup>[38]</sup> However, much of the research on ionogel has focused on heating/cooling outdoor operation or single functions.

Here, we constructed a multi-stage micro-structured multifunctional ionic skin (MM i-skin) with high sensitivity to address the problems of low sensitivity and dependence on exogenous drive of traditional sensors, which integrated nanogenerators and sensors in one body and achieved two working modes of piezoelectricity / thermoelectricity with the same material (**Figure 1**). And the microstructure template of the taro leaves and sandpaper were replicated by the bio-template method to build a multi-stage microstructured sensor. Then the obtained ion pressure sensor with papillary microstructured PDMS gold electrode and rough [EMIM]DCA ionogel dielectric layer, which featured a sensitivity of up to  $77.4 \text{ kPa}^{-1}$  below 1 kPa, a fast response time (46 ms), a wide pressure detection limit (1 kPa to 50 kPa), and a high cycle durability (over 1500 cycles), and it also can monitor the human physiological signals like breathing and pulse anytime. The prepared thermoelectric [EMIM]DCA ionogel with high Seebeck coefficient of  $11.435 \text{ mV}^{-1}$ , excellent ionic conductivity of  $8.55 \times 10^{-2} \text{ S cm}^{-1}$  and low thermal conductivity of  $0.2 \text{ W m}^{-1}\text{K}^{-1}$ , as well as an ionic power of  $0.12 \text{ }\mu\text{W}$ , and the output voltage reached 58.83 mV at temperature gradient of 5 K. To demonstrate the piezoelectric properties of ionogel, piezoresponse force microscopy (PFM) was adopted to demonstrate the corresponding voltage signals when the ionogel was pressed, and the ionic gradient would be created owing to the varying mobility of anions and cations, which can be explained by the ionic piezoelectric effect in the ionogel. By this way, the P-skin was produced and applied for real-time monitoring of human limb activity signals and robot motion recognition. Further, integrating thermoelectric nanogenerator and pressure sensor converts body temperature gap into voltage for self-powered wearable health monitoring. In summary, with its significant advantages of high sensitivity, multifunction, and self-power, the MM i-skin is expected to be adopted in smart medical system to achieve home-style self-health monitoring in real time (Figure 1).

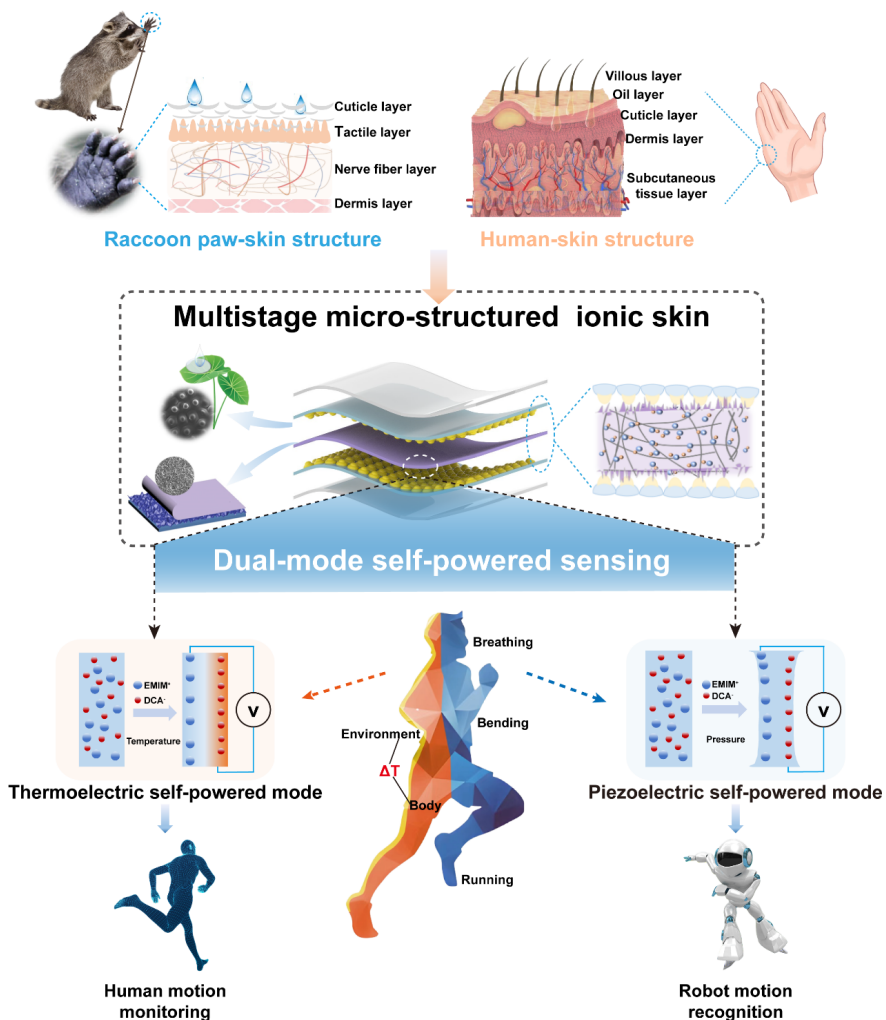


**Figure 1.** Schematic of design strategy and geometric morphology of the MM i-skin. Inspired by raccoon paw-skin and human-skin, the micro-level multi-stage “interlocked” configuration is designed for precise sensing and simultaneously integrating sensors with piezo / thermo-electricity dual-mode nanogenerator for self-powered monitoring and recognition.

## 2. Results and discussion

### 2.1. Preparation and characterizations of MM i-skin

MM i-skin device is designed as a classic sandwich-like structure, mainly composed of two key parts: PDMS thin film with papillary microstructure Au (PM-PDMS / Au) electrode and dielectric layers, which the upper and lower electrode layers are led out by copper wires, and the whole device is encapsulated by PI tape (**Figure 2 a**). Here, the microstructured PM-PDMS / Au electrode was prepared by a low-cost bio-template method, and the template method can well reproduce the original microstructure of plant leaves from SEM images of the surface of taro leaves (Figure 2b, Figure 2c, and Figure S2). The inset in Figure 2a shows the plan micrograph of the PM-PDMS / Au electrode and the microscopic enlarged image of a randomly selected single mastoid. And the insets in them display its longitudinal (with an average height of 17.01  $\mu\text{m}$ ) and transverse (with an average width of 11.8  $\mu\text{m}$ ) size distribution. The

PVDF-HFP containing [EMIM]DCA ionogel was prepared as the dielectric layer benefiting from its superior chemical stability, mechanical properties, and plasticity due to the existence of crystalline phase PVDF and amorphous HFP in PVDF-HFP,<sup>[39,40]</sup> the schematic diagram of its synthesis mechanism is shown in Figure 2d. The optical and microscopic images of the ionogel show that it has the typical porous structural characteristics of gel (Figure 2e, and the inset in it displays the groove microstructure of ionogel matching the papillary microstructure). And EDS elemental mapping reveals the exclusive distribution of nitrogen (N), which conforms to the elemental distribution characteristics of [EMIM]DCA ionogel, indicating that the ionic liquid has been successfully loaded and uniformly distributed in PVDF-HFP 3D networks (Figure 2f). The crystal structures and phase of [EMIM]DCA ionogel loaded with different amounts of ionic liquids were further researched by X-ray diffraction (XRD) (Figure 2g). XRD results show that the XRD patterns of pure PVDF-HFP at 17.9° and 19.5° correspond to the (100) and (110) planes of the PVDF-HFP $\alpha$ -phase.<sup>[41]</sup> In an ionogel with a [EMIM]DCA loading of 16 wt%, a new peak can be observed at 20.5° due to the (200) plane of the PVDF-HFP $\beta$ -phase.<sup>[42]</sup> This is consistent with the FTIR patterns (Figure 2h). When the [EMIM]DCA loading was further increased, the XRD pattern broadened and the intensity of these crystalline peaks decreased significantly, indicating that the crystallinity of PVDF-HFP in the ionogel decreased. While its corresponding crystalline peaks intensity when the loading was 24 wt% is higher, which also shows that the crystallinity of PVDF-HFP in the ionogel is relatively high under this ionic liquid content. This can be attributed to [EMIM]DCA-induced shrinkage of PVDF-HFP polymer chains. The FTIR spectra also reveals that the presence of ionic liquid significantly changes the crystal structure of PVDF-HFP (Figure 2h). The FTIR band of the characteristic peaks at 760 cm<sup>-1</sup> and 794 cm<sup>-1</sup> could be attributed to the  $\alpha$ -phase, while the peak at 838 cm<sup>-1</sup> can be attributed to the  $\beta$ -phase of PVDF-HFP.<sup>[43-45]</sup> While with the addition of different types of ionic liquids ([EMIM]CL, [EMIM]DCA, [EMIM]BF<sub>4</sub>), the  $\alpha$ -phase peak in PVDF-HFP weakened and the  $\beta$ -phase peak became more obvious. Among the three types of ionic liquids, the weakening of the  $\alpha$ -phase peak and the enhancement of the  $\beta$ -phase peak in PVDF-HFP added with [EMIM]CL-24 wt% are the most obvious, mainly due to the stronger ion-dipole interactions between Cl<sup>-</sup> and PVDF-HFP components. In addition, Figure S4 also provides details of the characteristic peaks of crystalline region, non-crystalline region and different ionic liquids in the PVDF-HFP form the FTIR spectra. The Raman spectra further reveals the interaction between anions and PVDF-HFP, among which [EMIM]DCA-24 wt% exhibits the strongest Raman spectra intensity, indicating that there is a strong interaction between [DCA]<sup>-</sup> ions and PVDF-HFP (Figure 2i). Such a result further revealed that the ionic liquid was successfully loaded into the PVDF-HFP network. Therefore, the PVDF-HFP based ionogel with a loading of 24 wt% [EMIM]DCA ionic liquid was adopted for subsequent studies.

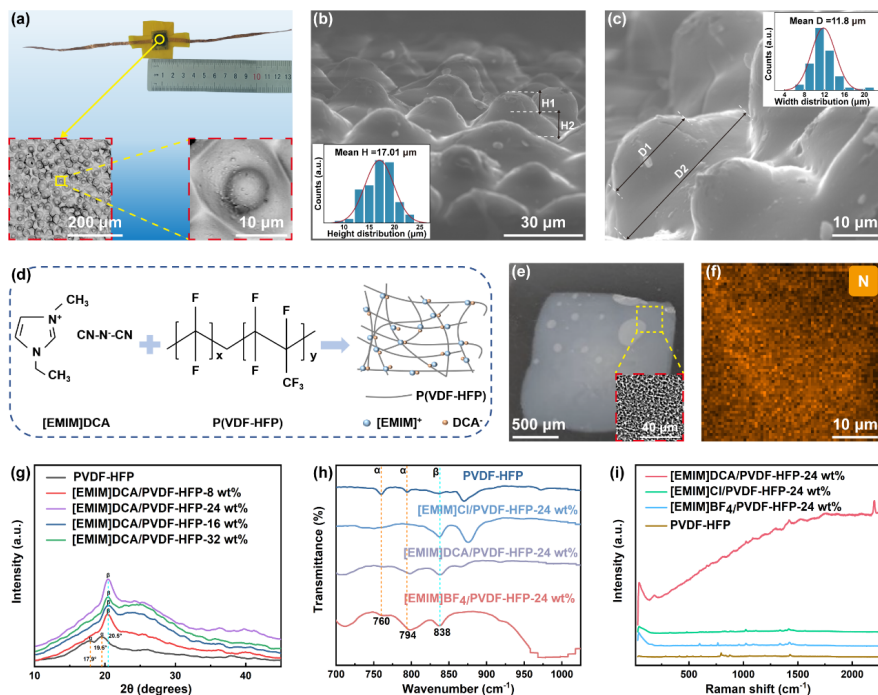


**Figure 2.** Characterizations of the PM-PDMS / Au electrode and ionogel. a) Optical images of the MM i-skin device (the inset shows the SEM images of the full-field and local zoom-in papillary gold electrodes). b-c) Cross-sectional SEM image of the PM-PDMS film at different magnifications (the inset illustrates the height and width size distribution of the PM-PDMS film bump). d) Schematic diagram of the internal crosslinking network and chemical structure of PVDF-HFP-based ionogel. e) Optical images of the ionogel (the inset displays the SEM images of the groove microstructure prepared by sandpaper template method). f) EDS elemental mapping of ionogel. g) X-ray diffraction patterns of PVDF-HFP and [EMIM]DCA ionogel loaded with different amounts of ionic liquids. h-i) Fourier infrared spectrum and Raman spectroscopy of PVDF-HFP-based ionogel loaded with different kinds of ionic liquids.

## 2.2. Capacitive ion skin with multi-stage microstructure (C-skin)

It has been found in previous studies that the existence of multi-level three-dimensional micro-nano structures can effectively improve the sensing performance of devices.<sup>[46,47]</sup> The cross-sectional schematic diagram of the C-skin structure shows a classic sandwich-like structure (**Figure 3 a-i**). In the initial state (**Figure 3a-ii**), the ionogel contains free-moving cations and anions without external pressure and voltage. When a voltage is applied (**Figure 3a-iii**), opposite charges on the electrodes attract ions in the ionogel layer, forming microscale capacitors with nanometre separation. This leads to ultra-high capacitance per unit area, as electron-ion pairs constitute the capacitor structure.<sup>[48]</sup> The equivalent circuit diagram indicates that the capacitance CEDL1 and CEDL2 formed between each of the upper, lower electrode layers and the ionogel are connected in series to equivalently constitute the capacitance of the entire device (**Figure S5**). This kind of electrical double layer capacitor can effectively improve its capacitance performance.<sup>[49]</sup>

Sensitivity, response time, pressure responsiveness, cyclic stability, and linear response are the most important sensing properties of the pressure sensor.<sup>[50]</sup> The response and reply curve of the C-skin when the stepper motor exerts a force of 2 kPa on the sensor exhibiting extremely short response time ( $\sim 46$  ms) and reply time ( $\sim 0.42$  s) (**Figure 3B**, and **Figure S6** provides an enlarged curve plots of response and recovery time for a single cycle), whose response time is the same as that of human skin (30-50 ms).<sup>[51]</sup> This extremely short response time can be ascribed to the special double-layered papillary microstructure electrode and the ionogel with suitable concentration and roughness. To elucidate that, the capacitive performance of

double-layered mastoid structure and interlocking capacitive sensors were further studied, proving that the interlocking capacitive sensors can effectively improve the capacitive response capability (Figure S7a). In the interlocking configurations consisting of ionogel with concave microstructure and double-layered mastoid microstructured electrodes, the effect of different surface roughness (0, 180, 600, 1000-grit) of ionogel on the capacitive sensing sensitivity was further studied in Figure S7b, the SEM image of which is shown in Figure S8. When the gel is formed on the 600-grit sandpaper, more pits with a diameter of about 20  $\mu\text{m}$  appeared on the surface, which was comparable to the size of the papillary microstructured electrodes, with which an interlocking configuration was well formed. As a result, the capacitive sensitivity of the interlocked configuration with the 600-grit sandpaper substrate inverted with ionogel as the dielectric layer was significantly better than the other three substrates. In addition, different concentrations of ionic liquids (8 wt%, 16 wt%, 24 wt%, and 32 wt%) was studied to explore the relationship between the ionic skin sensitivity and the ionic liquid concentration (Figure S9), which shows that the sensitivity of the double-layered capacitor sensors increases with the increase of ionic liquid concentration, the highest sensitivity was found at an ionic liquid concentration of 24 wt%. Owing to the establishment of the electrical double layer within the gel, the quantity of free  $[\text{EMIM}]^-$  and  $\text{DCA}^+$  increases as the ionic liquid content rises. When free electrons are present on both sides of the electrode, more anions and cations are attracted, leading to an increase in capacitance and a corresponding increase in sensitivity. However, excessive concentration of the ionic liquid (over 32 wt%) can cause the the adhesion of the dielectric layer to the electrode layer and poor recovery of the sensor, eventually resulting in a slight decrease in the sensitivity of the sensor. Therefore, the C-iskin composed of PVDF-HFP-based ionogel with a loading of 24 wt%  $[\text{EMIM}]\text{DCA}$  ionic liquid and a roughness of 600-grit exhibits high sensitivity of  $77.4 \text{ kPa}^{-1}$  below 1 kPa (Figure S9).

Pressure responsiveness is one of the criteria for evaluating sensing performance, the device was able to maintain a stable and reliable electrical signal even when in a pressure of 2, 8, and 30 kPa (Figure 3c, and Figure S10a also explores the minimum detection limit of the C-iskin). The results show that the C-iskin has a stable response, excellent matching between pressure and capacitance changes, high repeatability, and clear signals under various pressures. which is much higher than the conventional response range of human skin ( $<10 \text{ kPa}$ ). Furthermore, the deformation state of PM-PDMS films under different pressures (0 to 50 kPa) and maximum pressure detection limit of C-iskin was explored by means of simulation (Figure 3d). As the exerted force was gradually increased from 0 to 50 kPa (in steps of 10 kPa), the PM-PDMS films still maintained their original shape and the microstructures were not destroyed, which indicates the excellent stability of the sensor. And the rest of the deformation under different pressures was further studied (see Figure S11 for more details). In addition, the capacitance variation of the C-iskin shows excellent matching with different loading / unloading times and operating frequencies, ensures stable response and high repeatability of the C-iskin (in Figure S10b-d). In order to investigate the mechanical durability of the C-iskin, it was subjected to 1500 loading / unloading cycles at a pressure of 2 kPa. The results show that the C-iskin doesn't suffer from fatigue (Figure 3e), suggesting excellent repeatability, stability, and durability, and the two insets show that the waveform remains essentially unchanged at the beginning and the end of the cycle, with a slight increase in amplitude. In fact, the cycling curve amplitude as a whole exhibit a slight upward trend with the increase in the number of cycles, which attributed to the structural damage of the double-layered mastoid-like microstructures after prolonged loading / unloading cycles, resulting in a shortened distance between the two electrodes.

Stretchability and flexibility are the fundamental requirements to fulfill the wearable health monitoring devices. The mechanical properties of PM-PDMS films, ionogel films with different ionic liquid concentrations, and microstructured ionogel films obtained from the above preparations were analyzed (Figure S12). The results indicate the PDMS film can withstand 140% strain with a fracture strength of 1.2MPa, while PM-PDMS exhibits an unprecedented high fracture strength of 2.0MPa at 134% strain, which is increased by 60% (Figure S12a-b). The elongation at fracture of the two is similar, while the Young's modulus of PM-PDMS is 74% higher than that of PDMS. The results discussed above show that the introduction of microstructure plays an important role in improving the mechanical properties of C-iskin. Similarly, the analysis results of ionic liquid concentration (Figure S12c-d) and gel roughness (Figure S12e-f) show that  $[\text{EMIM}]\text{DCA}$ -24

wt% and 600 mesh have excellent comprehensive mechanical properties.

Thanks to the excellent integrated sensing capabilities of the C-skin, it has great potential in wearable health monitoring applications. C-skin was placed on the vocal cords, upper lip and wrist of the volunteers respectively to monitor vocalization, respiration and pulse signals, and its output curve shows that the above movements and signals can be easily and accurately detected (Figure 3f-h). Therefore, C-skin has important application prospects in health monitoring, robotic motion monitoring and prosthetics.

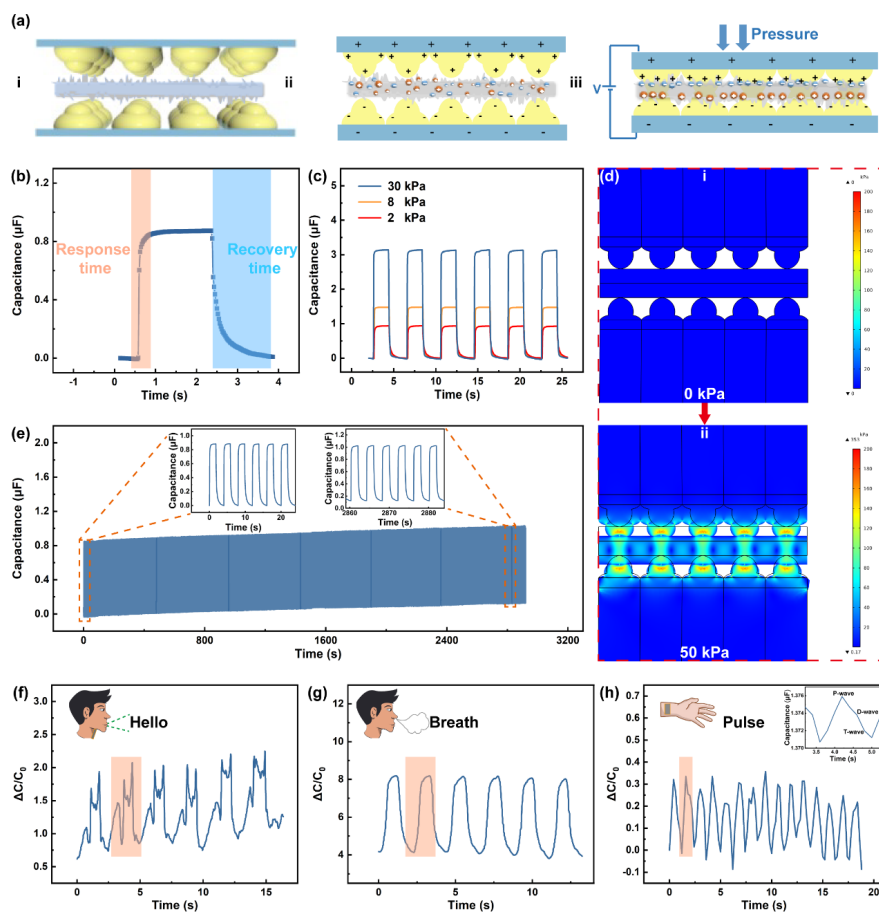


**Figure 3.** The structure design, working mechanism, performance and application scenarios of C-skin. a) The cross-sectional structure and working principle diagram. b) Response and recovery curve for a single cycle. c) Response curves at pressures of 2, 8, and 30 kPa. d) Simulation result at 0 and 50 kPa pressure. e) The cyclic curve of 1500 load and unload at 2 kPa and partial magnified curve. f) Voice monitoring. g) Respiratory monitoring. h) Pulse monitoring.

### 2.3. Ionogel thermoelectric nanogenerators

Further study of the thermoelectrochemical properties of PVDF-HFP-based ionogel was aimed at revealing their capability as thermoelectric self-powered monitoring devices. The working mechanism of thermoelectric ionogel is as illustrated in **Figure 4 a**. In the initial state (Figure 4a-i), there is an absence of internal temperature gradient, causing random distribution of anions and cations throughout the entire gel. This leads to a relatively low ionic concentration gradient and subsequently results in a lower ionic potential difference. Under a temperature gradient (Figure 4a-ii), the ions exhibit migration from the cold end to the hot end due to the ion thermal diffusion effect. Furthermore, the dissimilar radii of the anions  $[EMIM]^+$  and

[DCA]<sup>-</sup> contribute to distinct migration rates. This disparity in migration rates establishes a concentration gradient across the temperature gradient, culminating in the generation of a voltage. Over time, electrons will naturally diffuse from the hot end to the cold end within the external circuit when an external resistor is connected in series on both sides of the ionogel. When the external circuit is disconnected and the gel is left in an open circuit, the ion concentration gradient will be gradually reestablished due to the temperature difference, resulting in the restoration of voltage after a certain period of time (Figure 4a-iii).<sup>[37,52,53]</sup> Further, By performing CV scans on the ionogel at different rate (50, 100, 200, 400, 500, and 1000 mV/s), which shows the excellent electrochemical properties.

The properties of thermoelectric ionogel are usually evaluated by their Seebeck coefficients, which is measured by a customized thermoelectric test system in this work. Figure 4b demonstrates the S of the PVDF-HFP-based ionogel as a function of the three types of ionic liquid types and concentrations (loading capacity of 8 wt%, 16 wt%, 24 wt%, and 32 wt%). Apparently, the S of PVDF-HFP-based ionogel doped with [EMIM]DCA ionic liquids are significantly better than those of the other two types of ionic liquids. For [EMIM]DCA ionic liquids, the S exhibit a significant increase with increasing loading, reaching a maximum value of 11.435 mV K<sup>-1</sup> at the loading of 32 wt%. The ionic maximum conductivity of 8.55 mS cm<sup>-1</sup> was get when the ionic liquid loading was 32 wt% measured by the electrochemical workstation at room temperature (25 °C) (Figure S14a-c). The ionic conductivity of the ionogel can be calculated by taking the impedance value corresponding to the real part when the imaginary part is 0 and introducing the ionic resistance value R<sub>ion</sub>. And the Nyquist plot shows a straight line without the semicircular shape of typical polymer gels, which because of the dielectric relaxation of the ions as reported by some published reports. Thermal conductivity is one of the basic parameters for evaluating the performance of thermoelectric ionogel, and therefore it was investigated (Figure 4c). The thermal conductivity of [EMIM]DCA-32 wt% gel at 36 °C (the normal temperature of human skin) was measured to be 0.22 W m<sup>-1</sup>K<sup>-1</sup> using a thermal conductivity tester (the inset in Figure 4c shows the test principle of the Hot Disk method). Combined with another parameter, the thermoelectric figure of merit, which is usually used to evaluate the comprehensive performance of thermoelectric materials, the final result calculated shows that the thermoelectric figure of merit for this ionogel is as high as 0.11 (Figure 4c). In summary, the [EMIM]DCA / PVDF-HDF-32 wt% ionogel exhibited a large Seebeck coefficient, excellent ionic conductivity, thermal conductivity, and excellent thermoelectric conversion efficiency, which shows great potential as materials for making thermoelectric generators.

Therefore, the output voltage, current, and power were tested by externally loading different resistance values (200, 675, 1000, 2000, 10,000, and 20,000 Ω) (Figure 4d). It is obvious that as the external resistance increases, the output voltage gradually increases and the current gradually decreases. The maximum voltage is 30 mV and the minimum current is 1.5 μA when the external resistor is 20,000 Ω. The current value reaches a maximum of 11 μA while the external resistor is changed to 200 Ω, and the minimum voltage is 3 mV. Based on the above characteristics of output voltage and current under different resistive loads, the power curve is plotted (Figure 4e), from which it can be seen that the overall trend of the curve increases with the increase of the connection resistance, and when the resistance is increased to a specific value, the power curve peaks, i.e., the maximum output power, which decreases as the load resistance continues to increase. The maximum power reaches 0.12 μW when the external resistance is 675 Ω. The inset in Figure 4e shows a schematic diagram of the test equivalent circuit for an external load of thermoelectric ionogel. The output electrical performance tests were performed in the presence of a 5 K temperature difference, while the open-circuit voltages and short-circuit currents of the ionogel outputs at a temperature difference of 8 K were studied (Figure S15).

The thermoelectric conversion capability of the ionogel was examined by further heating / cooling cycle experiments (Figure 4f), it can be seen that the ionogel exhibits excellent thermoelectric responsiveness during a single heating / cooling cycle and the overall curve waveform are well behaved. However, there is a slight decrease in the overall amplitude of the curves, which may be attributed to the decrease in the thermoelectric potential due to the thermal hysteresis effect of the thermocouples and the material when it is heated, but overall, there is a reversible thermal voltage switching during the 5 repetitive heating / cooling cycles. The results of the I-V curves obtained by connecting test electrodes at both ends of the

ionogel and measuring its sensing performance under different pressures (Figure 4g). The resistance of the gel decreases linearly with increasing pressure due to an expansion of conductive channels within the ionogel and a decrease in ion spacing, which enables the ionogel to function as both pressure sensors and piezoelectric generators.

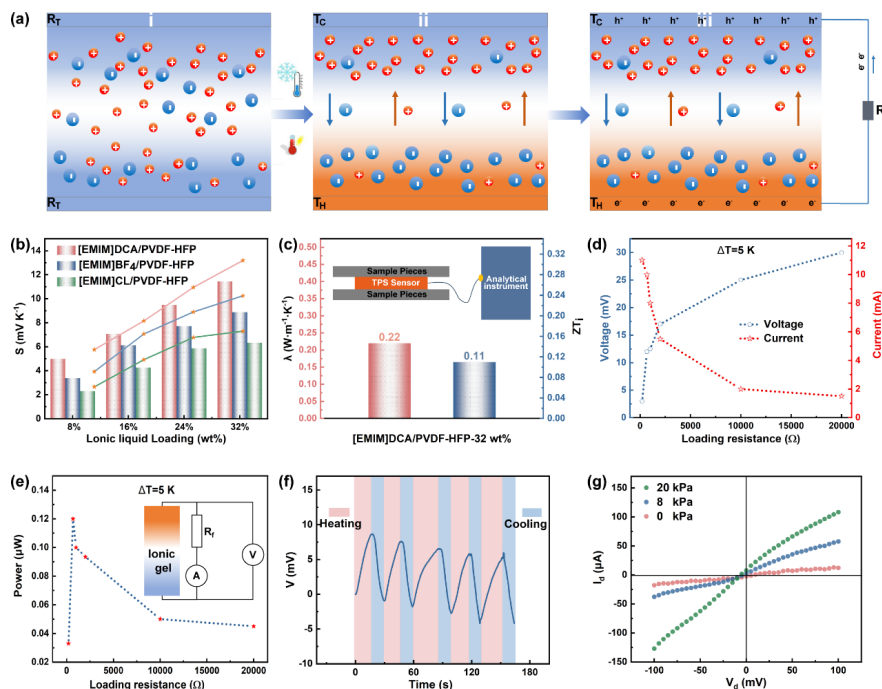


**Figure 4.** Working Principle and thermoelectrochemical performance of ionogel. a) Schematic diagram of the operation of an ionogel thermoelectric generator based on the ion thermoelectric effect. b) Seebeck coefficients for various types of ionic liquids and ionogel with different loading. c) Thermal conductivity and thermoelectric figure of merit of thermoelectric ionogel. d) Variation of output voltage and current with external resistance. e) Graph of output power with external resistance. f) Cyclic thermoelectric responsiveness during ionogel heating / cooling cycles. g) Thermoelectric ionogel I-V curve.

#### 2.4. Piezoelectric self-powered ion skin (P-iskin)

A self-powered piezoelectric ionic skin (P-iskin) was developed based on the ionic piezoelectric effect for human health monitoring. The ion piezoelectric effect of the sensor is caused by the migration of cations and anions in the ion film layer of the sensor when stimulated by external pressure (Figure 5 a).<sup>[48,54,55]</sup> The piezoelectric properties were verified by piezoresponse force microscopy (PFM) mode of atomic force microscope (AFM) (Figure 5b).<sup>[56,57]</sup> A strategically placed layer of copper tape has been introduced between the sample and the probe tip for two-fold purpose: i) it mitigates potential damage to the sample by curtailing high current density; ii) the employment of copper tape acts as an effective isolating barrier to avoid structural damage to flexible gels caused by probe tip. Therefore, Figure 5c is an AFM image of the copper strip surface and not of any other sample. The phase diagrams after loading forward (-5 V) and reverse (+5 V) bias voltages to the sample are given in the red curve (Figure 5d), clear hysteresis lines can be noticed from it, and the 180° reversal of the phase signal also reflects the existence of ferroelectric polarization in the ionogel. And the obvious butterfly curve can be seen from its amplitude graph as the blue curve (Figure 5d), after bias is added to the sample, voltage-induced deformation of the sample leads to cyclic vibrations on the sample surface, which are delivered to the probe tip and sensitively read out with the help of a lock-in amplifier (LIA).<sup>[56]</sup> This proves in reverse that the sample can convert the pressure signal into an electrical signal and reflect it in the form of a voltage signal under a certain pressure.

Next, we perform real-time detection and collection of force electrical signals through a customized set of linear motors, force transducers, high-precision digital source meters, and computer systems (the inset in Figure 5e). With a pressure of approximately 5 N provided by a linear stepper motor, the ion skin exhibits stable piezoelectric responsiveness. The results show that a voltage of approximately 250 mV can be output, with each waveform in the curve represents a loading / unloading cycle (Figure 5e). It is worth noting that the electrokinetic response curve exhibits an initial voltage in the absence of any pressure stimulation, which can be attributed to the abundance of free cations within the ionogel and the non-uniform distribution of positive and negative ions, even if the overall ion balance within the gel is relatively maintained.

Consequently, the ionogel demonstrates promising potential as a self-powered piezoelectric pressure sensor, rendering it suitable for monitoring human physiological signals. It effectively converts mechanical energy generated during human activities into electrical energy, which can be further translated into discernible electrical signals. An advanced ion-piezoelectric self-drive wearable health monitoring sensor (P-iskin) was developed, whose device structure parallels that of C-iskin (see the Figure S16 for its corresponding equivalent circuit diagram). The piezoelectric potential generated by the piezoelectric ion effect is regarded as the internal power supply to provide guarantee for the normal operation of the device.

Firstly, the P-iskin was employed to monitor the recovery motion generated by the arm activity of a volunteer who had undergone surgery for a fractured right arm three months ago. The volunteer executed a series of successive flexion-extension-flexion movements, with the corresponding output electrical signal curve displayed (Figure 5f). Each elevated peak observed in the curve represents a complete cycle, wherein a slight upward spike is noticeable, which can be attributed to muscle tremors that occur due to incomplete recovery of the bones following the surgical intervention. As a control measure, the P-iskin device was utilized to monitor the activity of the healthy left elbow joint of the volunteer. And it can be observed that the electrical signal curve for each action cycle exhibits exceptional smoothness, devoid of any spurious peaks (Figure 5g).

In addition, by placing P-iskin on the stationary elbow and performing clenched and relaxed fist motions with the right and left hand respectively (Figure S17a-b), it is used to monitor the recovery progress of the injured arm. It is evident from the action cycle of the right hand that muscle tremor persists in the injured hand and peaks are observed, whereas the left hand presents a relatively smooth pattern without any false peaks. P-iskin can be placed on skin scars and further used to monitor the recovery of injured skin growth in human body, which demonstrates the superior ability of P-iskin to monitor motion in normal skin and scarred skin. The above research demonstrates that the device can provide certain assistance for medical rehabilitation and guidance for building a wearable health monitoring system and family self-reconstruction, and avoid secondary harm to oneself during the reconstruction process.

With the rapid advancements in technology, wearable robots are undergoing remarkable progress and becoming increasingly prevalent in our daily lives. Our research has revealed that P-iskin holds immense promise in the realm of robotic action recognition (Figure S18). We securely attached the P-iskin to the robot's feet and proceeded to execute a series of maneuvers, including front and back somersaults, lateral sliding, and walking. Figure S18a presents the output signal diagram capturing the robot's somersaults. The illustration below displays the action signal detected by the P-iskin throughout an action cycle. Notably distinct, the variations in the output signal enable accurate judgment of the corresponding actions based on these discernible patterns. Figure S18b-c exhibits the step signals of the robot's lateral sliding and walking movements. Each peak corresponds to a distinct walking step, and the consistent shape of these peaks signifies the remarkable stability of P-iskin. This implies its potential for reliable recognition of the robot's walking states.

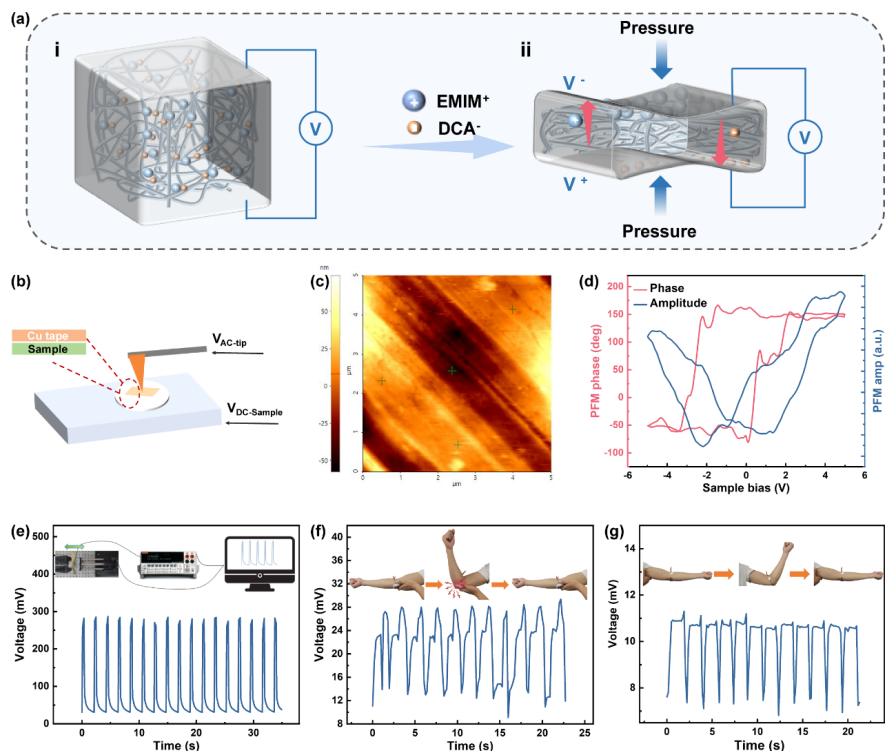


**Figure 5.** Characterization of piezoelectric properties of P-iskin. a) Schematic diagram of ion piezoelectric effect. b) Schematic of PFM test. c) Shape graph of AFM test including test points. d) Graphs of voltage versus phase and voltage versus amplitude after applying bias voltages to the sample for forward voltage ( $-5\text{ V}$ ) and reverse voltage ( $+5\text{ V}$ ). e) Characterization of piezoelectric properties using a customized force-electric test system. f) P-iskin for injured arm motion monitoring. g) P-iskin for healthy arm motion monitoring.

## 2.5. Thermoelectric self-powered ion skin (T-iskin)

Given the excellent thermoelectrochemical performance of the ionogel, a thermoelectric self-powered ion skin (T-iskin) was constructed for health monitoring (see the **Figure 6 a** for its explosion diagram of structure). The T-iskin harnesses its inherent thermoelectric effect, enabling it to function as a self-powered source for strain detection, eliminating the requirement for an external power supply.  $R_f$  is the load resistor in parallel, and the change in output voltage of the thermoelectric pressure sensor is reflected by testing the relative resistance change of this resistance (Figure 6b), which is obviously easy to see that by applying different pressure (2, 8, and 30 kPa), the relative resistance change of the load resistor changes significantly.

As commonly acknowledged, humans are homoiothermal creatures with a typical body temperature of approximately  $37^\circ\text{C}$ . During winter, the standard room temperature ranges from  $18^\circ\text{C}$  to  $25^\circ\text{C}$ , while in summer, it varies from  $23^\circ\text{C}$  to  $28^\circ\text{C}$ . Consequently, the temperature gradient is easily generated by the differences between the body's temperature and that of the surrounding environment. The ionogel previously studied can generate a voltage of about  $75\text{ mV}$  and a current of about  $25\text{ }\mu\text{A}$  at a temperature of  $8\text{ K}$  (Figure S14), which can be used to drive the T-iskin for the monitoring of human physiological movements. Self-powered and synchronized sensing capabilities in natural environments were further demonstrated by a T-iskin attached to a finger (Figure 6c-i). As the fingers perform a sequential motion cycle of straightening-bending-stretching, each peak in the signal output curve detected by T-iskin represents a finger movement, facilitating precise identification of individual finger activity. Thus, it holds potential for monitoring the health status of the knuckles. Similarly, the T-iskin is placed on the wrist and calf to detect the movement action (Figure 6c-

ii-iii), and the results show that the waveform and amplitude in the curves are well maintained, and the voltage signals possess an excellent match with the movement. Motion monitoring from the above three physiological sites revealed different peaks and peak shapes of motion signals in varied sites, which were related to the temperature of the place and the force during action. This research offers a research basis for the utilization of low-order thermal energy in the human body.

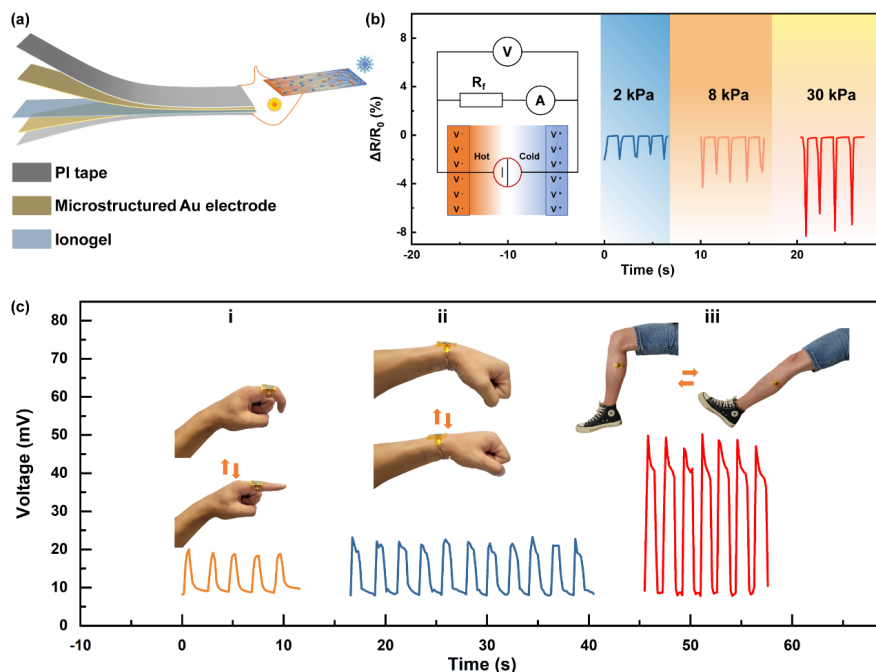


**Figure 6.** Characterization and performance of T-iskin. a) Structure diagram of T-iskin. b) Working principal diagram of T-iskin. c) T-iskin acts as a pressure sensor to recognize movement signals from fingers, wrist and calf. The inset shows the specific actions during detection.

### 3. Conclusion

In summary, we construct a multistage micro-structured multifunctional ionic skin (MM i-skin) that features high sensitivity, excellent responsiveness (46 ms), great durability, and its superior sensing performance has been vastly improved over previous pressure ionic skin. As a capacitive function ionic skin (C-iskin), it was initially applied to monitor subtle vital physiological signals including breathing, voice recognition, and pulse. As the outstanding contribution of this work, a self-powered wearable health monitoring device using different properties of the same material to achieve two different energy supply modes was devised, that is piezoelectric self-powered ion skin (P-iskin) and thermoelectric self-powered ion skin (T-iskin), aiming at eliminating dependence on external power supply. P-iskin shows great potential for real-time monitoring of human joint activities. Furthermore, the T-iskin based on the low-order thermal energy from the temperature difference between the human body and the environment, which is used for real time monitoring of human joint activities. Therefore, the utilization of own low-order energy proposed in this study provides great reference significance for the construction of self-powered wearable health monitoring devices as well as solving the energy crisis, realizing real-time self-health monitoring and the building of smart medical systems.

## 4. Experimental Section

*Materials:* Poly (methacrylate (PMMA, 98.5%), Polydimethylsiloxane (PDMS, 85%), Trichloromethane ( $\text{CHCl}_3$ , 99%), Poly vinylidene fluoride-hexafluoro propylene (PVDF-HFP, 99%), 1-ethyl-3-methylimidazolium dicyanamide (EMIM[DCA], 99%). Taro leaf (Produced in Yuxi City, Yunnan Province), Sand paper. All chemicals were of analytical purity and used directly without any processing, except for taro leaves and sandpaper that have been cleaned.

*Preparation of PDMS electrodes:* PDMS electrodes were prepared by plant template method combined with electron beam deposition (Figure S1). The PMMA particles are mixed with trichloromethane at a mass ratio of 8:100 and stirred until completely dissolved, and then the prepared PMMA solution was applied dropwise to the surface of fresh taro leaves then heating at 60 for 1 h. The PMMA film was peeled off from the leaf as a PMMA template with the opposite structure of the taro. Next, the PDMS precursor solution was mixed with the curing agent (10:1) and smeared onto the above PMMA template then heating at 60 for 2 h. Then, the PDMS film was peeled off from the PMMA template to obtain the PDMS film with taro leaf papillary microstructure (PM-PDMS), and the PMMA template was cleaned and dried naturally for recycling and reusing. Finally, the microstructured gold electrode (with the Au film thickness of 250 nm) was prepared by electron beam evaporation, which was denoted as PM-PDMS / Au.

*Preparation of ionogel dielectric layers:* Ionogel with different roughness were prepared by sandpaper reverse mold (Figure S3). After completely dissolving 0.2 g PVDF-HFP in 2.5 ml acetone solution, 0.2 ml, 0.4 ml, 0.6 ml, and 0.8 ml EMIM[DCA] ionic liquids were added to the same four PVDF-HFP solutions, respectively, which were recorded as EMIM[DCA]-8 wt%, EMIM[DCA]-16 wt%, EMIM[DCA]-24 wt%, and EMIM[DCA]-32 wt%, and stirred vigorously to ensure the uniform mixing of ionic liquid and PVDF-HFP. Then a little of the above-configured mixed solution was applied onto the sandpaper with different roughness, heating at 60 °C for 2 h to obtain ionogel film possessing rough surface. Furthermore, a slide of smooth ionogel film was selected as a substrate for contrastive analysis.

*Assembly of flexible ion pressure sensor:* The flexible ion pressure sensor was designed as sandwich-like structure where the PM-PDMS / Au film acts as the upper and lower electrodes and the ionogel was employed as the dielectric layer film, and the copper wire was used as a test electrode. Further, the electrical double layer capacitive ion pressure sensor can be encapsulated with PI film (Figure 1).

*Characterization and measurements:* SEM morphological and elemental characterization of PDMS and PVDF films was performed by the Phenom Pro X. Characterization of the mechanical properties of PDMS films and ionogel was exerted using a universal material testing machine (UTM 4000, Shenzhen Suns Co. Ltd, China). By controlling the stepper motor to provide different pressures, the performance of the capacitive pressure sensor at low frequencies is tested with the Victor 4091C precision LCR meter, and the capacitive sensing performance at high frequencies is measured by Keithley 4200 SCS semiconductor parameter tester. Electrochemical workstation (CHI-660e, Shanghai Chenhua Co. Ltd, China) was employed to test the electrochemical impedance spectra and cyclic voltammetric curves of all the samples. The ionic conductivity of the ionogel can be calculated from obtained electrochemical impedance spectroscopy data. Thermal conductivity monitoring of ionogel was measured by Hot Disk TPS 2500 S thermal conductivity meter; The thermoelectric performance of ionogel was characterized by the customized thermoelectric test system (refer to the published work).<sup>[58]</sup>

## Acknowledgements

X.W. and J.Z. contributed equally to this work. This work was financially supported by the National Natural Science Foundation of China (No. 52271241 and 52071282) and the National Training Programs of Innovation and Entrepreneurship for Undergraduates (No. 202210673068 and 202210673002). Authors thank Advanced Analysis and Measurement Center of Yunnan University for the sample testing service and Ad-

vanced Computing Center of Yunnan University. The authors thank the software support from Prof. Hai Yang from Kunming University.

## Conflict of Interest

The authors declare no conflict of interest.

## Supporting Information

Supporting Information is available from the Wiley Online Library or from the author.

## Keywords

skin-like microstructure, bio-template method, ionic skin, dual-mode self-powered, integrated device

Received: Revised: Published online:

### References

- [1] J. R. DiPalma, R. McMichael, M. DiPalma, *Science (New York, N.Y.)* **1966** , 152, 539.
- [2] N. Chen, R. Rink, H. Zhang, presented at 1995 IEEE/RSJ International Conference on Intelligent Robots and Systems - Human Robot Interaction and Cooperative Robots, Pittsburgh, Pa, Aug 05-09, **1995** .
- [3] J. Dargahi, S. Najarian, *Int. J. Med. Robot. Comput. Assist. Surg.* **2004** , 1, 23.
- [4] G. Lee, J. Son, D. Kim, H. J. Ko, S. G. Lee, K. Cho, *Small* **2022** , 18, 9.
- [5] T. Hagihara, H. Mano, T. Miura, M. Hasebe, M. Toyota, *Nat. Commun.* **2022** , 13, 9.
- [6] J. Gould, *Nature* **2018** , 563, S84.
- [7] R. S. Dahiya, G. Metta, M. Valle, G. Sandini, *IEEE Trans. Robot.* **2010** , 26, 1.
- [8] J. Park, Y. Lee, J. Hong, Y. Lee, M. Ha, Y. Jung, H. Lim, S. Y. Kim, H. Ko, *ACS Nano* **2014** , 8, 12020.
- [9] C. Jeong, H. Ko, H. T. Kim, K. Sun, T. H. Kwon, H. E. Jeong, Y. B. Park, *ACS Appl. Mater. Interfaces* **2020** , 12, 18813.
- [10] M. Ha, S. Lim, J. Park, D. S. Um, Y. Lee, H. Ko, *Adv. Funct. Mater.* **2015** , 25, 2841.
- [11] Y. N. Hao, Q. Y. Yan, H. J. Liu, X. Y. He, P. H. Zhang, X. H. Qin, R. R. Wang, J. Sun, L. M. Wang, Y. Cheng, *Adv. Funct. Mater.* **2023** , DOI: 10.1002/adfm.20230388112.
- [12] J. Q. Wang, B. H. Wu, P. Wei, S. T. Sun, P. Y. Wu, *Nat. Commun.* **2022** , 13, 12.
- [13] W. Wang, Y. Jiang, D. Zhong, Z. Zhang, S. Choudhury, J. C. Lai, H. Gong, S. Niu, X. Yan, Y. Zheng, C. C. Shih, R. Ning, Q. Lin, D. Li, Y. H. Kim, J. Kim, Y. X. Wang, C. Zhao, C. Xu, X. Ji, Y. Nishio, H. Lyu, J. B. H. Tok, Z. Bao, *Science* **2023** , 380, 735.
- [14] J. L. Guo, C. Q. Xiang, A. Conn, J. Rossiter, *Soft Robot.* **2020** , 7, 309.
- [15] M. K. Kim, J. H. Cho, H. B. Shin, S. W. Lee, Ieee, presented at 11th International Winter Conference on Brain-Computer Interface (BCI), Tech Univ Berlin, Korea Univ Inst Artificial Intelligence, ELECTRONETWORK, Feb 20-22, **2023** .

- [16] K. Zhou, S. Wang, L. Xu, H. Li, Y. Wang, Z. Qiu, G. Zhang, Z. Zhao, B. Z. Tang, *Matter* **2023** , 6, 3449.
- [17] L. Chen, R. L. Li, S. L. Yuan, A. P. Chen, Y. Li, T. Zhang, L. Wei, Q. C. Zhang, Q. W. Li, *Matter* **2023** , 6, 925.
- [18] L. M. Wang, N. Li, Y. F. Zhang, P. J. Di, M. K. Li, M. Lu, K. Liu, Z. H. Li, J. Y. Ren, L. Q. Zhang, P. B. Wan, *Matter* **2022** , 5, 3417.
- [19] H. S. Niu, S. Gao, W. J. Yue, Y. Li, W. J. Zhou, H. Liu, *Small* **2020** , 16, 12.
- [20] T. Yang, W. L. Deng, X. Chu, X. Wang, Y. T. Hu, X. Fan, J. Song, Y. Y. Gao, B. B. Zhang, G. Tian, D. Xiong, S. Zhong, L. H. Tang, Y. H. Hu, W. Q. Yang, *ACS Nano* **2021** , 15, 11555.
- [21] F. Basarir, Z. Madani, J. Vapaavuori, *Adv. Mater. Interfaces* **2022** , 9, 18.
- [22] Q. X. Liu, Y. Liu, J. L. Shi, Z. G. Liu, Q. Wang, C. F. Guo, *Nano-Micro Lett.* **2022** , 14, 12.
- [23] H. S. Niu, H. Li, S. Gao, Y. Li, X. Wei, Y. K. Chen, W. J. Yue, W. J. Zhou, G. Z. Shen, *Adv. Mater.* **2022** , 34, 11.
- [24] K. Q. Xia, Z. Y. Zhu, H. Z. Zhang, Z. W. Xu, *Appl. Phys. A-Mater. Sci. Process.* **2018** , 124, 7.
- [25] L. Zhao, S. H. Yu, J. J. Li, Z. C. Song, M. Y. Wu, X. Y. Wang, X. H. Wang, *Curr. Appl. Phys.* **2021** , 31, 29.
- [26] H. Hu, D. R. Wang, H. M. Tian, Q. Y. Huang, C. H. Wang, X. L. Chen, Y. Gao, X. M. Li, X. M. Chen, Z. J. Zheng, J. Y. Shao, *Adv. Funct. Mater.* **2022** , 32, 9.
- [27] J. C. Li, J. Yin, M. G. V. Wee, A. Chinnappan, S. Ramakrishna, *Adv. Fiber Mater.* **2023** , 5, 1417.
- [28] D. Choi, Y. Lee, Z. H. Lin, S. M. Cho, M. Kim, C. K. Ao, S. Soh, C. Sohn, C. K. Jeong, J. W. Lee, M. B. Lee, S. A. Lee, J. Ryu, P. Parashar, Y. J. Cho, J. Ahn, I. Kim, F. Jiang, P. S. Lee, G. Khandelwal, S. J. Kim, H. S. Kim, H. C. Song, M. Kim, J. Nah, W. Kim, H. G. Menge, Y. T. Park, W. Xu, J. H. Hao, H. Park, J. H. Lee, D. M. Lee, S. W. Kim, J. Y. Park, H. X. Zhang, Y. L. Zi, R. Guo, J. Cheng, Z. Yang, Y. N. Xie, S. M. Lee, J. H. Chung, I. Oh, J. S. Kim, T. H. Cheng, Q. Gao, G. Cheng, G. Q. Gu, M. Shim, J. H. Jung, C. W. Yun, C. Zhang, G. X. Liu, Y. F. Chen, S. Kim, X. Y. Chen, J. Hu, X. Pu, Z. H. Guo, X. D. Wang, J. Chen, X. Xiao, X. Xie, M. Jarin, H. L. Zhang, Y. C. Lai, T. Y. Y. He, H. Kim, I. Park, J. Ahn, N. D. Huynh, Y. Yang, Z. L. Wang, J. M. Baik, D. Choi, *ACS Nano* **2023** , 17, 11087.
- [29] Y. H. Jia, Q. L. Jiang, H. D. Sun, P. P. Liu, D. H. Hu, Y. Z. Pei, W. S. Liu, X. Crispin, S. Fabiano, Y. G. Ma, Y. Cao, *Adv. Mater.* **2021** , 33, 46.
- [30] L. H. Li, M. M. Hao, X. Q. Yang, F. Q. Sun, Y. Y. Bai, H. Y. Ding, S. Q. Wang, T. Zhang, *Nano Energy* **2020** , 72, 9.
- [31] L. H. Li, Z. G. Chen, M. M. Hao, S. Q. Wang, F. Q. Sun, Z. G. Zhao, T. Zhang, *Nano Lett.* **2019** , 19, 5544.
- [32] G. D. Fan, K. K. Liu, H. Su, Y. Q. Luo, Y. Geng, L. Y. Chen, B. J. Wang, Z. P. Mao, X. F. Sui, X. L. Feng, *Chem. Eng. J.* **2022** , 434, 11.
- [33] J. M. Ma, S. A. Firdosy, R. B. Kaner, J. P. Fleurial, V. A. Ravi, *J. Mater. Sci.* **2014** , 49, 1150.
- [34] Y. Gelbstein, G. Gotesman, Y. Lishzinker, Z. Dashevsky, M. P. Dariel, *Scr. Mater.* **2008** , 58, 251.
- [35] T. Watanabe, E. Oe, Y. Mizutani, T. Ono, *Soft Matter* **2023** , 19, 2745.
- [36] B. W. Yang, W. Yuan, *ACS Appl. Mater. Interfaces* **2019** , 11, 16765.
- [37] K. K. Liu, J. C. Lv, G. D. Fan, B. J. Wang, Z. P. Mao, X. F. Sui, X. L. Feng, *Adv. Funct. Mater.* **2022** , 32, 12.

- [38] Z. Q. Shen, X. Y. Zhu, C. Majidi, G. Y. Gu, *Adv. Mater.***2021** , 33, 12.
- [39] Shalu, S. K. Chaurasia, R. K. Singh, S. Chandra, *J. Phys. Chem. B* **2013** , 117, 897.
- [40] W. Chen, Z. Xing, Y. Wei, X. Y. Zhang, Q. G. Zhang, *Polymer* **2023** , 268, 10.
- [41] P. Martins, A. C. Lopes, S. Lanceros-Mendez, *Prog. Polym. Sci.* **2014** , 39, 683.
- [42] Z. Sha, C. Boyer, G. Li, Y. Y. Yu, F. M. Allieux, K. Kalantar-Zadeh, C. H. Wang, J. Zhang, *Nano Energy* **2022** , 92, 15.
- [43] H. L. Cheng, X. He, Z. Fan, J. Y. Ouyang, *Adv. Energy Mater.* **2019** , 9, 7.
- [44] Y. Bormashenko, R. Pogreb, O. Stanevsky, E. Bormashenko, *Polym. Test* **2004** , 23, 791.
- [45] G. R. Peng, X. J. Zhao, Z. J. Zhan, S. Z. Ci, Q. Wang, Y. J. Liang, M. L. Zhao, *RSC Adv.* **2014** , 4, 16849.
- [46] S. J. Han, C. R. Liu, Z. B. Huang, J. W. Zheng, H. H. Xu, S. Chu, J. Wu, C. Liu, *Adv. Mater. Technol.* **2019** , 4, 9.
- [47] Q. F. Du, L. L. Liu, R. T. Tang, J. Ai, Z. J. Wang, Q. Q. Fu, C. X. Li, Y. Chen, X. Feng, *Adv. Mater. Technol.* **2021** , 6, 8.
- [48] W. Li, J. Zhang, J. R. Niu, X. Jin, X. M. Qian, C. F. Xiao, W. Y. Wang, *Nano Energy* **2022** , 99, 13.
- [49] S. Gong, W. Schwalb, Y. W. Wang, Y. Chen, Y. Tang, J. Si, B. Shirinzadeh, W. L. Cheng, *Nat. Commun.* **2014** , 5, 8.
- [50] Y. Bao, J. C. Xu, R. Y. Guo, J. Z. Ma, *Prog. Chem.***2023** , 35, 709.
- [51] K. Tao, J. H. Yu, J. Y. Zhang, A. C. Bao, H. W. Hu, T. Ye, Q. L. Ding, Y. Z. Wang, H. B. Lin, J. Wu, H. L. Chang, H. X. Zhang, W. Z. Yuan, *ACS Nano* **2023** , 17, 16160.
- [52] J. H. Chen, L. Zhang, Y. Y. Tu, Q. Zhang, F. Peng, W. Zeng, M. Q. Zhang, X. M. Tao, *Nano Energy* **2021** , 88, 8.
- [53] C. Liu, Q. K. Li, S. J. Wang, W. S. Liu, N. X. Fang, S. P. Feng, *Nano Energy* **2022** , 92, 9.
- [54] Y. Liu, Y. Hu, J. J. Zhao, G. Wu, X. M. Tao, W. Chen, *Small* **2016** , 12, 5074.
- [55] C. Lu, X. Chen, *Chem. Phys. Lett.* **2022** , 803, 5.
- [56] X. Xu, T. T. Zhong, N. Zuo, Z. X. Li, D. Y. Li, L. J. Pi, P. Chen, M. H. Wu, T. Y. Zhai, X. Zhou, *ACS Nano* **2022** , 16, 8141.
- [57] Y. C. Wang, L. M. Vu, T. Lu, C. L. Xu, Y. Liu, J. Z. Ou, Y. X. Li, *ACS Appl. Mater. Interfaces* **2020** , 12, 51662.
- [58] Z. Q. Zhou, Y. F. Wan, J. Y. Zi, G. M. Ye, T. S. Jin, X. M. Geng, W. B. Zhuang, P. Yang, *Mater. Today Sustain.* **2023** , 21, 9.

#### Hosted file

Figure.docx available at <https://authorea.com/users/767780/articles/826833-multistage-micro-structured-ionic-skin-for-real-time-vital-signs-monitoring-and-human-machine-interaction>